文章编号：1001-9014(2025)01-0033-07

DOI:10.11972/j.issn.1001-9014.2025.01.005

A HgTe/ZnO quantum dots vertically stacked heterojunction low dark current photodetector

HUANG Xin-Ning[1,2], JIANG Teng-Teng[1,2], DI Yun-Xiang[1], XIE Mao-Bin[1,2], GUO Tian-Le[1*], LIU Jing-Jing[1], WU Bin-Min[1], SHI Jing-Mei[4], QIN Qiang[4], DENG Gong-Rong[4], CHEN Yan[1], LIN Tie[1], SHEN Hong[1], MENG Xiang-Jian[1], WANG Xu-Dong[1], CHU Jun-Hao[1,2], GE Jun[1*], WANG Jian-Lu[3]

(1. State Key Laboratory of Infrared Physics, Shanghai Institute of Technical Physics, Chinese Academy of Sciences, Shanghai 200083, China;
2. University of Chinese Academy of Sciences, Beijing 100049, China;
3. Frontier Institute of Chip and System, Institute of Optoelectronics, Shanghai Frontier Base of Intelligent Optoelectronics and Perception, Fudan University, Shanghai 200438, China;
4. Kunming Institute of Physics, Kunming 650223, China)

Abstract: Colloidal quantum dots (CQDs) are affected by the quantum confinement effect, which makes their bandgap tunable. This characteristic allows these materials to cover a broader infrared spectrum, providing a cost-effective alternative to traditional infrared detector technology. Recently, thanks to the solution processing properties of quantum dots and their ability to integrate with silicon-based readout circuits on a single chip, infrared detectors based on HgTe CQDs have shown great application prospects. However, facing the challenges of vertically stacked photovoltaic devices, such as barrier layer matching and film non-uniformity, most devices integrated with readout circuits still use a planar structure, which limits the efficiency of light absorption and the effective separation and collection of photo-generated carriers. Here, by synthesizing high-quality HgTe CQDs and precisely controlling the interface quality, we have successfully fabricated a photovoltaic detector based on HgTe and ZnO QDs. At a working temperature of 80 K, this detector achieved a low dark current of 5.23×10^{-9} A cm^{-2}, a high rectification ratio, and satisfactory detection sensitivity. This work paves a new way for the vertical integration of HgTe CQDs on silicon-based readout circuits, demonstrating their great potential in the field of high-performance infrared detection.

Key words: colloidal quantum dots, photodetector, barrier layer, heterojunction

HgTe/ZnO量子点垂直堆叠异质结低暗电流光电探测器

黄新宁[1,2], 姜腾腾[1,2], 狄云翔[1], 谢茂彬[1,2], 郭天乐[1*], 刘晶晶[1], 吴斌民[1], 施静梅[4], 秦 强[4], 邓功荣[4], 陈 艳[1], 林 铁[1], 沈 宏[1], 孟祥建[1], 王旭东[1], 褚君浩[1,2], 葛 军[1*], 王建禄[3]

(1. 中国科学院上海技术物理研究所 红外物理国家重点实验室,上海 200083;
2. 中国科学院大学,北京 100049;
3. 复旦大学 芯片与系统前沿技术研究院,上海 200438;
4. 昆明物理研究所,云南 昆明 650223)

摘要:胶体量子点(CQDs)受量子限域效应的影响,其带隙具有可调谐的特性,因此该类材料能够覆盖更宽的

Received date: 2024-03-20, **revised date**: 2024-08-20　　**收稿日期**:2024-03-20,**修回日期**:2024-08-20

Foundation items: Supported by National Key Research and Development Program in the 14th five year plan (2021YFA1200700), Strategic Priority Research Program of the Chinese Academy of Sciences (XDB0580000), Natural Science Foundation of China (62025405, 62104235, 62105348).

Biography: HUANG Xin-Ning (1996-), male, Jiangxi, Ph. D. candidate. His main research area is the synthesis of HgTe CQDs and its application in photodetectors. E-mail: huangxinning@mail.sitp.ac.cn

* **Corresponding authors**: E-mail: guotianle@mail.sitp.ac.cn; Wonderge@163.com

红外光谱范围,为突破传统红外探测器的技术路线提供了一种高成本效益的替代方案。近年来,得益于量子点的溶液加工特性以及其与硅基读出电路的单芯片集成能力,基于碲化汞胶体量子点的红外探测器展现出极大的应用前景。然而,面对垂直堆叠光伏器件的挑战,如阻挡层的匹配和薄膜非均匀性等问题,当前大部分与读出电路集成的器件仍采用平面结结构,限制了光吸收效率以及光生载流子的有效拆分和收集。在这里,我们通过合成高质量碲化汞量子点及精准控制界面质量,成功制备了基于HgTe和ZnO量子点材料的光伏型探测器。该探测器在80 K的工作温度下,实现了低至5.23×10^{-9} A·cm^{-2}的暗电流水平和较高的整流比,以及满意的探测灵敏度。这项工作为碲化汞量子点在硅基读出电路上的垂直集成开辟了新途径,展示了其在高性能红外探测领域的巨大潜力。

关 键 词:胶体量子点;光电探测器;阻挡层;异质结

中图分类号:O475 **文献标识码**:A

Introduction

Infrared imaging technology plays a pivotal role across a diverse range of applications, spanning both defense and public sectors. This technology is crucial in areas such as medical diagnostics, nocturnal surveillance, security operations, environmental observation, pollutant detection, and molecular characterization[1-4]. Traditionally, the development of infrared detectors has been dominated by epitaxial materials such as Mercury Cadmium Telluride[5] and Indium Gallium Arsenide[6], as well as Indium Antimonide[7]. These materials are highly valued for their excellent sensitivity and performance across different infrared wavelengths. However, the complex manufacturing processes, high costs associated with epitaxial growth, and the need for cryogenic cooling systems to achieve optimal performance have focused their application range on military and industrial[8]. Over the last ten years, CQDs have seen remarkable advancements in the field of photodetection[9]. The appeal of CQDs lies in their size-tunable optical properties, which span the entire infrared spectrum, their cost-effectiveness in production, and their compatibility with direct application onto silicon readout integrated circuits (ROIC) for imaging purposes[10-13]. Consequently, CQDs hold the promise of significantly lowering the overall cost of sensors to nearly that of the silicon substrates they are applied to, while also introducing versatile new approaches to detector manufacturing.

However, current photodetectors based on HgTe CQDs, such as homojunction[14], photoconductive[15], trap-state photoconductive[11], planar p-n junction[16], and diode types[17], tend to exhibit high dark current. Planar p-n junctions in two-dimensional materials are commonly fabricated through the regulation by ferroelectric polarization fields[18-20]. These issues may arise from several factors: the spatial charge region of planar p-n junctions occupies a low proportion, the mismatch in barrier layer materials for diodes, and the insufficient density of the quantum dot films. Therefore, to develop a vertically stacked device structure with low dark current for integration with ROIC, it is crucial to address the selection of barrier layers, the quality of quantum dot synthesis, and the fabrication of high-quality thin films.

In this work, leveraging previously reported high-quality quantum dot synthesis and superlattice-like thin film fabrication techniques[21], and identifying ZnO QDs as a barrier layer, we have fabricated a HgTe/ZnO type-II heterojunction photodetector. Heterojunctions, compared to homojunctions, possess more abundant band information, allowing for the design of higher barriers, thereby more effectively suppressing dark current. This device demonstrates high rectification ratios and low dark currents at both room and low temperatures, presenting significant potential for future integration with ROIC.

1 Results and discussions

Figure 1(a) presents a detailed schematic of the device architecture, illustrating the HgTe CQDs/ZnO QDs heterostructure. The fabrication process involved the precise patterning of Ti/Au (5 nm/10 nm) metal electrodes using ultraviolet lithography, followed by deposition through electron beam evaporation. Subsequently, ZnO QDs were carefully deposited onto the pre-patterned electrodes and spin-coated at 2000 r/min for 30 seconds. The resulting film underwent annealing at 200 ℃ on a heating plate in ambient conditions for 1 hour. Next, the HgTe CQDs film was uniformly blade-coated onto the ZnO film and then subjected to heating at 45 ℃ for 5 minutes. Finally, a 70 nm indium tin oxide film was precisely deposited using dual ion beam sputtering to serve as the top transparent electrodes. In Figure 1(b) and 1(c), atomic force microscope (AFM) images provide a detailed view of the surface morphology of the HgTe and ZnO films, respectively. The HgTe film exhibits a surface roughness of 2.69 nm, indicative of a relatively smooth and compact surface. Similarly, the ZnO film displays a surface roughness of 577 pm, suggesting a uniform and flat surface conducive to forming a high-quality interface between the two materials. Figure 1(d) and 1(e) showcase the absorption spectra of HgTe and ZnO, respectively. The observed cutoff wavelengths are 3600 nm for HgTe and 370 nm for ZnO, indicating their respective absorption characteristics. This suggests that the fabricated heterojunction device is capable of responding to infrared radiation. Figure 1 (f) provides a comprehensive X-ray photoelectron spectroscopy (XPS) analysis of ZnO nanostructures. The O 1s peak observed in ZnO QD can be decomposed into two distinct subpeaks. The subpeak at a higher binding energy (approximately 531.48 eV) is associated with absorbed water (O−H), while the subpeak at a lower binding energy (approximately 530.06 eV) is

indicative of ZnO (O－Zn). Additionally, the peaks corresponding to Zn $2p_{\frac{3}{2}}$ and Zn $2p_{\frac{1}{2}}$ are found at 1 044.40 eV and 1 021.32 eV, respectively.

For energy level characterization, Figure 2 presents the ultraviolet photoelectron spectroscopy of the ZnO film and HgTe film. The work function (W_F) values of ZnO and HgTe are determined as 6.33 eV and 3.64 eV, respectively, using the equation $W_F = h\upsilon - E_{cut}$, where $h\upsilon$ = 21.2 eV represents the photon energy of He Ⅰ light. The cutoff energy (E_{cut}) values for ZnO and HgTe are measured as 14.87 eV and 17.56 eV, respectively, as depicted in Fig. 2(a) and 2(c). Furthermore, the Fermi levels of ZnO and HgTe are observed to be positioned 0.82 eV and 0.17 eV higher than the valence bands, as illustrated in Fig. 2(b) and 2(d). Additionally, based on the bandgap values calculated from the absorption spectrum, the conduction band (E_C) values are estimated to be 3.8 eV and 3.47 eV for ZnO and HgTe, respectively.

In accordance with the band information of each material, we depicted a schematic diagram of the band alignment for the heterojunction device, fabricating a type-II heterojunction as shown in Fig. 3(a). When HgTe CQDs absorb incident light to produce excitons, under the separation by the built-in electric field, electrons flow from HgTe to ZnO and are collected through the gold electrode, while holes flow from ZnO to HgTe and are collected through the ITO. The optical photograph of our detector is displayed in Figure 3(b), with the effective working area of the device being 100 μm × 100 μm. To investigate the interface conditions of our fabricated device, we conducted scanning electron microscopy (SEM) imaging of the device's cross-section, obtaining a clear image of the cross-section, as shown in Figure 3(c), the interfaces between each layer are clearly visible. The clean interface of the heterojunction device, prepared with overlapping smooth films, provides potential for effective optoelectronic detection.

To thoroughly assess the performance of the HgTe/ZnO heterostructure device, the figures of merit were carefully measured. We first tested the device's photodetection capability at room temperature, as shown in Fig. 4. Figure 4(a) shows the current density-voltage (*J-V*) curves of the device with power density varying from 0 to 9 W cm^{-2} under a 520 nm laser illumination. The device demonstrated a high rectification ratio of near five orders of magnitude at ±0.75 V in the dark state, suggesting minimal series resistance and effective charge extraction[22]. Under reverse bias, the photocurrent closely follows a smooth curve, indicating that the photogenerated carriers are effectively collected under the influence of an external electric field. This smooth curve and high rectification ratio are crucial in practical applications, as any abnormal voltage fluctuations near the operating bias from the ROIC would cause negligible interference to the signal intensity, thereby enabling real imaging. Figure 4(b) illustrates the relationship between photocurrent and incident light power under self-driven conditions, where they follow a power-law relationship given by $I_{ph} = P^{\alpha}$, α calculated to be 0.98 through exponential fitting. The near-ideal value of α suggests that defects in the device minimally affect the generation and recombination of photogenerated electron-hole pairs, attributed to the near-

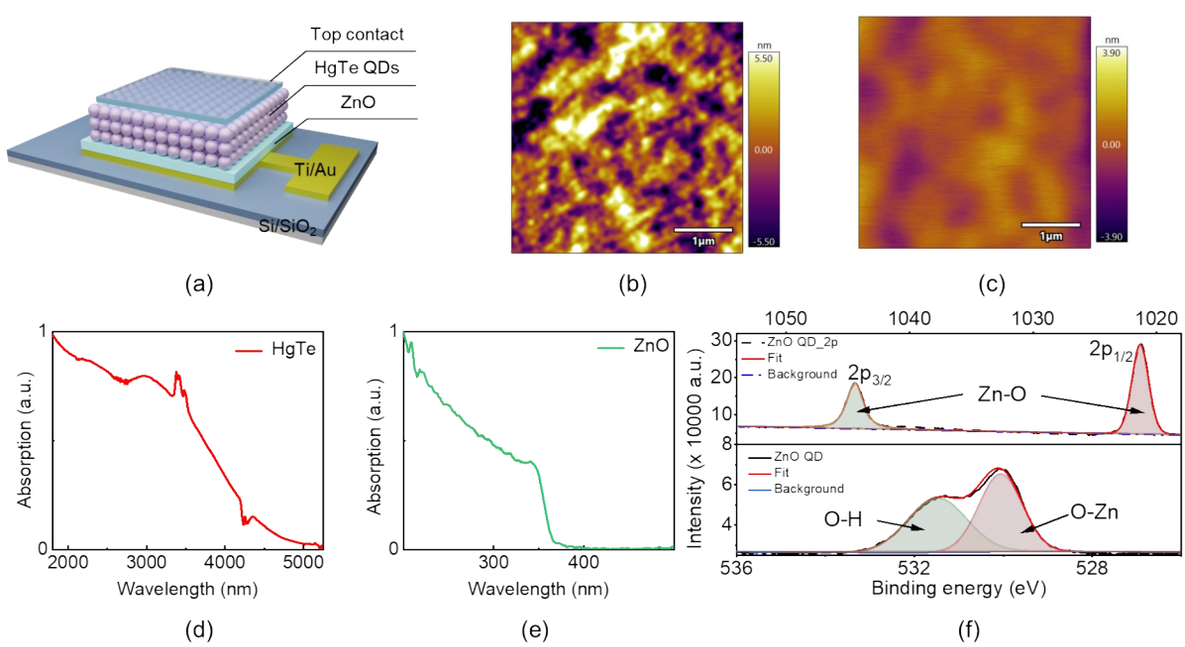

Fig. 1 Basic physical characteristics of materials: (a) device structure diagram of HgTe/ZnO heterojunction; (b) the AFM image of HgTe film; (c) the AFM image of ZnO film; (d) the absorption spectrum of HgTe film; (e) the absorption spectrum of ZnO film; (f) XPS spectra of Zn 2p and O 1s orbitals of ZnO thin films

图 1 材料的基本物理特性:(a) HgTe/ZnO 异质结的器件结构示意图;(b) HgTe 薄膜的 AFM 图像;(c) ZnO 薄膜的 AFM 图像;(d) HgTe 的吸收光谱;(e) ZnO 的吸收光谱;(f) ZnO 薄膜的 Zn 2p 和 O 1s 轨道的 XPS 光谱

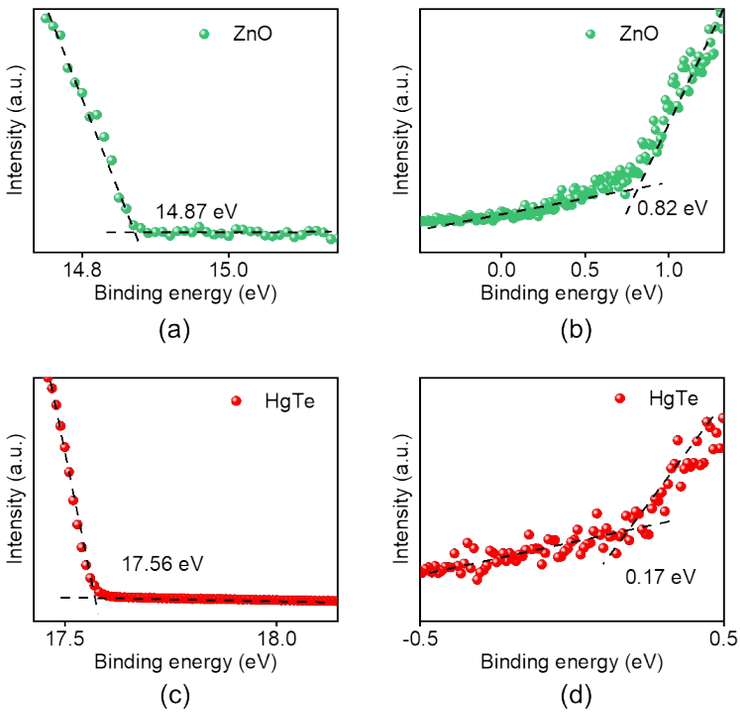

Fig. 2 The UPS of HgTe CQDs and ZnO QDs: (a)-(b) Valence band spectrum and second electron cutoffs of ZnO; (c)-(d) Valence band spectrum and second electron cutoffs of HgTe

图2 HgTe CQDs和ZnO QDs的紫外光电子能谱:(a)-(b) ZnO的价带电子能谱和二次电子截止边能谱;(c)-(d) HgTe的价带电子能谱和二次电子截止边能谱

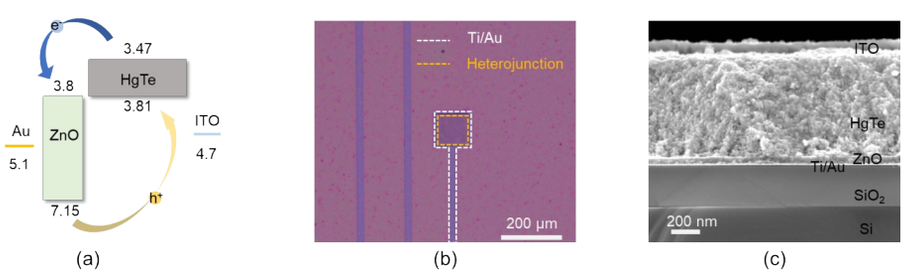

Fig. 3 The HgTe CQDs/ZnO QDs heterojunction: (a) Energy band diagram of the device; (b) the optical image of device; (c) the Cross-sectional SEM image of device

图3 HgTe CQDs/ZnO QDs异质结:(a) 器件能带示意图;(b) 器件光学照片;(c) 器件横截面的SEM图像

perfect interfaces in our fabricated device[23]. Another important parameter is the linear dynamic range (LDR), representing the stability of the photodetector's response rate under varying light intensities. The formula for calculating LDR is $\mathrm{LDR} = 20\log\frac{P_{sat}}{P_{low}}$, where P_{sat} and P_{low} are the maximum and minimum light intensities, respectively, at which the photocurrent deviates from the linear range. Here, the LDR of the heterojunction is around 34 dB, which limited by the varying power range of illumination of laser.

In the realm of photodetection, a short response time indicates the device's ability to quickly adapt to changes in light signals. Typically, response time refers to the time needed for excess carriers to recombine and for the device to recover from both shallow- and deep-level defects. Figure 4(c) illustrates that the falling and rising times, measured between 10% and 90% of the maximum photocurrent, are 455 μs and 410 μs, respectively. In addition, in the self-powered state, the -3 dB bandwidth is 1800 Hz as shown in Fig. 4(d).

Further characterization tests were conducted on our fabricated devices at the temperature of liquid nitrogen cooling (80 K). Figure 5(a) illustrates the device's *J-V* curves in dark state and under illumination of infrared laser at 80 K. It is observed that our device achieves a high rectification ratio close to three orders of magnitude in the dark state. This indicates a substantial enhancement in device performance, emphasizing the effectiveness of the design and materials used in achieving efficient charge separation and rectification in low-temperature conditions. However, for the rectifying characteristics of the device, from the high-temperature n-p junction to the low-temperature p-n junction, this is all attrib-

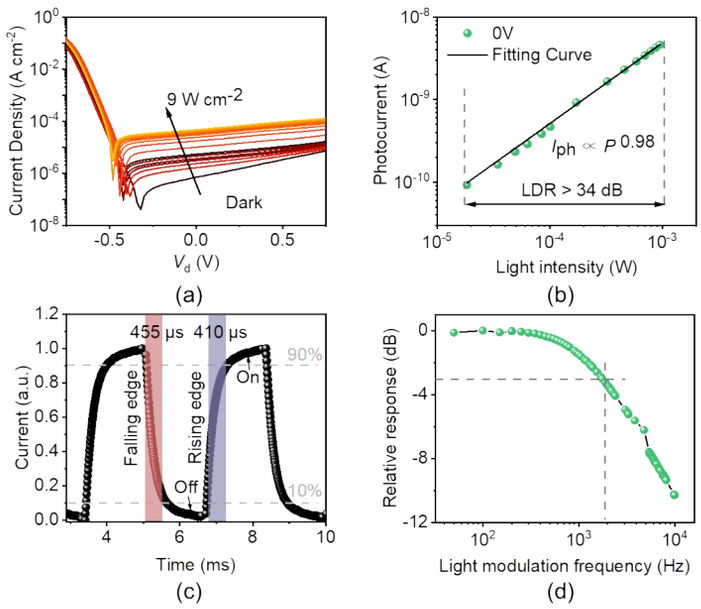

Fig. 4 The photoelectric properties at room temperature: (a) the output characteristic curve of the HgTe/ZnO heterojunction detector under 520 nm laser illumination with power varying from 0 to 9 W cm^{-2}; (b) the linear dynamic response range of the HgTe/ZnO heterojunction detector at 0 V; (c) the transient response of the HgTe/ZnO heterojunction detector at 0 V; (d) the response bandwidth of the HgTe/ZnO heterojunction detector

图 4 室温下光电特性:(a) HgTe/ZnO 异质结探测器在 520 nm 激光照射下功率从 0 到 9 W cm^{-2}的输出特性曲线;(b) HgTe/ZnO 异质结探测器在 0 V 下的线性动态响应范围;(c) HgTe/ZnO 异质结探测器在 0 V 下的瞬态响应;(d) HgTe/ZnO 异质结探测器的响应带宽

uted to the change in the position of the material's energy bands with temperature[24,25]. At 1 V bias, the dark current density is as low as 5.23 nA cm^{-2}, which is nearly four orders of magnitude lower compared to under 1625 nm laser illumination. This is significantly lower than the dark current reported for most devices based on HgTe CQDs, as summarized in Table 1. Notably, the dark current remains almost unchanged within the voltage range of -2 V to 1 V, attributing to the excellent interface between layers and the role of the ZnO layer as an effective hole-barrier layer. It efficiently transports electrons while blocking holes over a wide range of up to 3 V, which is crucial for real-world applications, ensuring device functionality is not affected by minor external voltage fluctuations

The noise level of the device is also an important indicator for the practical application of photodetectors. Our device was encapsulated in a Dewar, and the relationship between current noise and frequency under a 1 V bias was tested using a preamplifier and spectrum analyzer, as shown in Fig. 5(b). At lower frequencies, the current noise decreases with increasing frequency due to the predominant 1/f noise. At higher frequencies (>10 kHz), the current noise stabilizes around 2×10^{-17} A Hz$^{-1/2}$. Extracting data from Fig. 5a, with a device area of 100 μm × 100 μm, we obtain a dark current value of 5.23×10^{-13} A under a 1 V bias, and a photocurrent value of 1.44×10^{-9} A under 1 625 nm laser illumination at 90 μW power. The net photocurrent, calculated as $I_{ph} = I_{light} - I_{dark}$, equals 1.44×10^{-9} A. The responsivity of the photodetector, defined as $R = \frac{I_{ph}}{P}$, is calculated to be 16 μA W^{-1}. The specific detectivity, an important metric for photodetectors, is defined by the formula $D^* = \frac{R\sqrt{A}}{i_n}$, where A is the device area and i_n is the root mean square current noise at a bandwidth of 1 Hz. The specific detectivity of our device is calculated to be 8×10^9 cm Hz$^{1/2}$ W^{-1}.

Understanding the mechanism of dark current is crucial for photodetectors. We tested the relationship between dark current and temperature, ranging from 80 K to 280 K, as shown in Fig. 5(c). As the temperature decreases, the device's dark current gradually reduces. This is mainly due to the logarithm of the thermal carrier density n_i being directly proportional to the reciprocal of the temperature $\frac{1}{KT}$, i.e., $\ln(n_i) \propto \frac{1}{KT}$[26]. As the temperature decreases, the thermal carrier density n_i exponentially decreases with the increase of $\frac{1}{KT}$. Additionally, at low temperatures, some defects in the quantum dots are frozen, reducing the possibility of non-radiative recombination and increasing the carrier lifetime, thereby leading to a reduction in dark current. The relationship between the detector's dark current and temperature can be expressed as: $J_{dark} = C\exp(\frac{-E_a}{KT})$, where C is a temperature-independent factor, K is the Boltzmann constant, and E_a is the activation energy obtained from the Arrhenius fit of the temperature-dependent dark current. The Arrhenius fit, as shown in Fig. 5(d), yields an activation energy E_a of 0.315 eV above the crossover temperature T_c=180 K, slightly less than the bandgap of HgTe CQDs, indicating that the dark current at higher tempera-

tures is primarily dominated by diffusion current.

Table 1 Dark current level comparison based on different HgTe CQDs device structures
表1 基于HgTe CQDs不同器件结构的暗电流水平对比

Device	T(K)	Dark current (A cm^{-2})	Ref
HgTe CQDs homojunction	80	5×10^{-6}	[14]
HgTe CQDs planer p-n junction	300	1×10^{-7}	[16]
HgTe CQD/SnO_2 diode	300	1×10^{-6}	[27]
HgTe CQD/ZnO heterojunction	80/300	5.23×10^{-9}/9×10^{-8}	This work

3 Conclusions

In summary, we have successfully developed a HgTe CQDs and ZnO QDs heterojunction photodetector, which showcases exceptional rectification characteristics similar to those observed in p-n junctions. The superior performance of this heterojunction photodetector is primarily due to the meticulous preparation of each thin film layer, ensuring uniformity, and the seamless integration at the interfaces between these layers. This meticulous fabrication process has yielded a device with excellent optoelectronic properties and a robust response to photonic stimuli. Tested under ambient conditions with a 520 nm laser, it demonstrated fast response and wide operational range, making it versatile for optical sensing and imaging. At low temperatures (80 K), it showed high sensitivity and low noise, ideal for precision applications. Variable temperature tests revealed its stable performance at higher temperatures due to diffusion-driven dark current, suggesting broad environmental adaptability. The simple integration method also hints at potential for easy scalability and complementary metal oxide semiconductor compatibility, promising for commercial high-tech applications and bridging lab research with practical use.

References

[1] Tang X, Ackerman M M, Chen M, *et al*. Dual-band infrared imaging using stacked colloidal quantum dot photodiodes[J]. *Nat. Photonics*, 2019, **13**: 277-282.

[2] Jiao H, Wang X, Chen Y, *et al*. HgCdTe/black phosphorus van der Waals heterojunction for high-performance polarization-sensitive midwave infrared photodetector[J]. *Sci. Adv*, 2022, 8: eabn1811.

[3] Zhang S, Huang X, Chen Y, *et al*. Black Arsenic Phosphorus Mid-Wave Infrared Barrier Detector with High Detectivity at Room Temperature[J]. *Adv. Mater.*, 2024, **36**.

[4] Qian SHI, Shu-Kui Z, Jian-Lu W, *et al*. Progress on nBn infrared detectors[J]. J. *Infrared Millim. Waves*, 2022, **41**: 139-150.

[5] Wang X, Wang M, Liao Y, *et al*. Molecular-beam epitaxy-grown HgCdTe infrared detector: Material physics, structure design, and device fabrication[J]. *SCI CHINA PHYS MECH*, 2023, **66**: 237302.

[6] Ying Y, Hong-Zhen W, Liu-Yan FAN, *et al*. Study on Molecular Beam Epitaxy of High indium InGaAs Films[J]. J. *Infrared Millim. Waves*, 2022, **41**: 987-994.

[7] Tong J, Luo H, Suo F, *et al*. Epitaxial indium antimonide for multi-band photodetection from IR to millimeter/terahertz wave[J]. *Photon. Res.*, 2022, **10**: 1194-1201.

[8] Liu J, Liu P, Chen D, *et al*. A near-infrared colloidal quantum dot imager with monolithically integrated readout circuitry[J]. *Nat. Electron*, 2022, **5**: 443-451.

[9] Guyot-Sionnest P, Ackerman MM and Tang X. Colloidal quantum dots for infrared detection beyond silicon [J]. *J. Chem. Phys*, 2019, **151**.

[10] Shen G, Chen M and Guyot-Sionnest P. Synthesis of Non-Aggregating HgTe Colloidal Quantum Dots and the Emergence of Air-Stable n-Doping[J]. J. *Phys. Chem. Lett*, 2017, 7b00775.

[11] Zhang S, Bi C, Qin T, *et al*. Wafer-Scale Fabrication of CMOS-

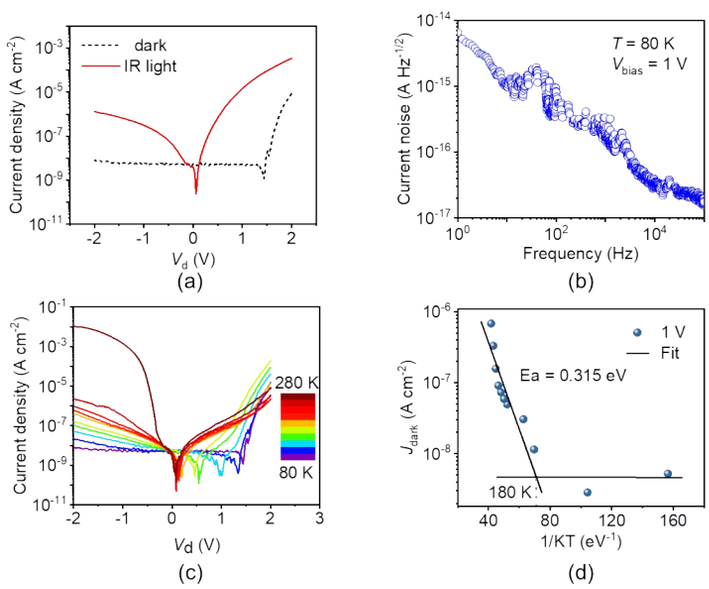

Fig. 5 The photoelectric properties at low temperatures: (a) the output characteristic curves of the HgTe/ZnO heterojunction detector at 80 K under dark conditions and under illumination by a 1 625 nm laser; (b) the relationship between current noise and frequency for the HgTe/ZnO heterojunction detector at 80 K with a 1 V bias voltage; (c) the variable temperature output characteristic curves of the HgTe/ZnO heterojunction detector in the dark state; (d) the Arrhenius fitting graph of the HgTe/ZnO heterojunction detector under a bias voltage of 1 V

图5 低温下光电特性:(a) HgTe/ZnO异质结探测器在80 K下的暗态和1 625 nm激光照射下的输出特性曲线;(b) HgTe/ZnO异质结探测器在80 K、1 V偏置电压下的电流噪声和频率的关系;(c) HgTe/ZnO异质结探测器暗态下的变温输出特性曲线;(d) 偏置电压1 V下,HgTe/ZnO异质结探测器的阿伦尼乌兹拟合图

Compatible Trapping-Mode Infrared Imagers with Colloidal Quantum Dots[J]. *ACS Photonics*, 2023,**10**:673-682.
[12] Alchaar R, Khalili A, Ledos N, et al. Focal plane array based on HgTe nanocrystals with photovoltaic operation in the short-wave infrared[J]. Appl. Phys. Lett, 2023,123:051108.
[13] Yang J, Lyu Y, He Z, *et al*. Bi2S3 Electron Transport Layer Incorporation for High-Performance Heterostructure HgTe Colloidal Quantum Dot Infrared Photodetectors[J]. *ACS Photonics*, 2023,**10**:2226-2233.
[14] Xue X, Chen M, Luo Y, *et al*. High-operating-temperature mid-infrared photodetectors via quantum dot gradient homojunction [J]. *Light Sci. Appl*, 2023,**12**:2.
[15] Luo Y, Tan Y, Bi C, *et al*. Megapixel large-format colloidal quantum-dot infrared imagers with resonant-cavity enhanced photoresponse[J]. *APL Photonics*, 2023,**8**:056109.
[16] Qin T, Mu G, Zhao P, *et al*. Mercury telluride colloidal quantum-dot focal plane array with planar p-n junctions enabled by in situ electric field - activated doping[J]. *Sci. Adv*, 2023,9:eadg7827.
[17] Gréboval C, Izquierdo E, Abadie C, *et al*. HgTe Nanocrystal-Based Photodiode for Extended Short-Wave Infrared Sensing with Optimized Electron Extraction and Injection[J]. *ACS Appl. Nano Mater*, 2022,**5**:8602-8611.
[18] Chen Y, Wang X, Huang L, *et al*. Ferroelectric-tuned van der Waals heterojunction with band alignment evolution [J]. *Nat. Commun*, 2021,**12**:4030.
[19] Jiao H, Wang X, Wu S, *et al*. Ferroelectric field effect transistors for electronics and optoelectronics[J]. *Appl. Phys. Rev*, 2023,**10**:
[20] Wu S, Chen Y, Wang X, *et al*. Ultra-sensitive polarization-resolved black phosphorus homojunction photodetector defined by ferroelectric domains[J]. *Nat. Commun*, 2022,**13**:3198.
[21] Huang X, Qin Y, Guo T, *et al*. Long-Range Hot-Carrier Transport in Topologically Connected HgTe Quantum Dots[J]. *Adv. Sci.*, 2024, **11**:2307396.
[22] Di Y, Ba K, Chen Y, *et al*. Interface Engineering to Drive High-Performance MXene/PbS Quantum Dot NIR Photodiode [J]. *Adv. Sci.*, 2024,**11**:2307169.
[23] Chen Y, Wang X, Wu G, *et al*. High-Performance Photovoltaic Detector Based on MoTe2/MoS2 Van der Waals Heterostructure [J]. *Small*, 2018,**14**:1703293.
[24] Klingshirn C. ZnO: Material, Physics and Applications[J]. *ChemPhysChem*, 2007,**8**:782-803.
[25] Dey P, Paul J, Bylsma J, *et al*. Origin of the temperature dependence of the band gap of PbS and PbSe quantum dots[J]. *Solid State Communications*, 2013,**165**:49-54.
[26] Sze S.M., Ng K.K. Physics and Properties of Semiconductors—A Review. In Physics of Semiconductor Devices (eds S.*M. Sze and K.K. Ng*). https://doi.org/10.1002/9780470068328.ch1
[27] Greboval C, Darson D, Parahyba V, *et al*. Photoconductive focal plane array based on HgTe quantum dots for fast and cost-effective short-wave infrared imaging[J]. *Nanoscale*, 2022,**14**:9359-9368.